Dalton Transactions

ROYAL SOCIETY OF CHEMISTRY

PAPER

View Article Online
View Journal | View Issue

Cite this: *Dalton Trans.*, 2021, **50**, 18143

Magnetic behavior of the novel pentagonal-bipyramidal erbium(III) complex $(Et_3NH)[Er(H_2DAPS)Cl_2]$: high-frequency EPR study and crystal-field analysis†

Lena Spillecke, *[a] Changhyun Koo,[a] Olga Maximova,[b] Vladimir S. Mironov,*[c,d] Vycheslav A. Kopotkov, [c] Denis V. Korchagin, [c] Alexander N. Vasiliev, [b,e] Eduard B. Yagubskii*[c] and Rüdiger Klingeler *[a,f]

Received 22nd September 2021,
Accepted 21st November 2021

DOI: 10.1039/d1dt03228c

rsc.li/dalton

We report the synthesis, crystal structure and magnetic properties of the new heptacoordinated mononuclear erbium(III) complex $(Et_3NH)[Er(H_2DAPS)Cl_2]$ (H_4DAPS = 2,6-diacetylpyridine bis-(salicylhydrazone)) (**1**). The coordination polyhedron around the Er(III) ion features a slightly distorted pentagonal bipyramid formed by the pentagonal N_3O_2 chelate ring of the H_2DAPS ligand in the equatorial plane and two apical chloride ligands. Detailed high-frequency/high-field electron paramagnetic resonance (HF-EPR) studies of **1** result in the precise determination of the crystal field (CF) splitting energies (0, 290 and 460 GHz) and effective *g*-values of the three lowest Kramers doublets (KDs) of the Er(III) ion. The obtained HF-EPR data are in good agreement with the results from CF analysis for the Er(III) ion based on the simulation of the dc magnetic data of **1**. The results from dynamic susceptibility measurements indicate that there is no slow relaxation of magnetisation behaviour. This observation is discussed in terms of the electronic structure of **1** obtained from experimental and theoretical results.

1 Introduction

Single-molecule-magnets (SMMs) have attracted a great deal of interest due to their forward-looking applications in ultra-high density data storage, quantum computing and molecular spintronics.[1–9] SMMs are magnetically bistable high-spin molecules with slow magnetic relaxation behaviour, capable of fixing magnetization below a certain blocking temperature T_B. Early SMM research (following the discovery of the first SMM $Mn_{12}Ac$ in 1993 [10]) was concentrated on polynuclear high-spin 3d coordination compounds.[11] After the discovery of slow magnetic relaxation behaviour in the mononuclear lanthanide complexes $[Pc_2Ln]^-$ with high spin-reversal barriers U_{eff} (Pc = phthalocyanide, Ln = Tb or Dy),[12] the focus has shifted to lanthanide SMMs, especially to mononuclear lanthanide complexes termed as single-ion magnets (SIMs).[13–18] In Ln-based SIMs, the barrier U_{eff} is controlled solely by the crystal field (CF) of 4f-electrons resulting from the ligand environment of the central Ln(III) ion, without spin coupling with other magnetic centers. Lanthanide complexes with strong axial CF display very high SMM characteristics. Currently, the record barriers (U_{eff} > 1500 cm^{-1}) and blocking temperature (T_B = 60–80 K) belong to low-coordinate (pseudo-linear) metallocene dysprosium complexes[19,20] and pentagonal-bipyramidal (PBP) Dy(III) complexes.[21] Their maximum SMM characteristics originate from the interplay of the large CF splitting energy of the lowest $^6H_{15/2}$ multiplet of Dy(III) ion (>1000 cm^{-1}) and strict axial symmetry of the CF potential, which is quantified by the three axial CF terms B_{20}, B_{40}, B_{60} and zero (or very small) non-axial terms B_{kq} with $q \neq 0$. In this case, the ground state of Dy(III) ion is the $m_J = \pm 15/2$ Kramers doublet (KD) with the most axial *g*-tensor (g_x = 0.00, g_y = 0.00 and $g_z \approx 20$) and exited Kramers doublets are strictly axial states with pure $m_J = \pm M$ values and Ising-type *g*-tensors (g_x = 0.00, g_y = 0.00 and $g_z > 0$). In this CF regime, strong axiality of KDs suppresses the quantum tunneling mechanism (QTM) of magnetic relaxation both in the ground state $m_J = \pm 15/2$ and in exited states $m_J = \pm M$ thereby max-

[a]*Kirchhoff Institute for Physics, Heidelberg University, INF 227, D-69120 Heidelberg, Germany. E-mail: lena.spillecke@kip.uni-heidelberg.de, r.klingeler@kip.uni-heidelberg.de*
[b]*Lomonosov Moscow State University, Moscow 119991, Russia*
[c]*Institute of Problems of Chemical Physics, RAS, Chernogolovka 142432, Russia. E-mail: yagubski@icp.ac.ru*
[d]*Shubnikov Institute of Crystallography of Federal Scientific Research Centre 'Crystallography and Photonics', RAS, Moscow 119333, Russia. E-mail: mirsa@list.ru*
[e]*National University of Science and Technology "MISiS", Moscow 119049, Russia*
[f]*Centre for Advanced Materials (CAM), Heidelberg University, Germany*

†Electronic supplementary information (ESI) available. CCDC 2099114. For ESI and crystallographic data in CIF or other electronic format see DOI: 10.1039/d1dt03228c

imizing the effective energy barrier U_{eff} to the upper CF energy levels lying above 1000 cm^{-1}.[19–21] However, all of these complexes can hardly be used as building blocks in polymetallic SMM assemblies due to lability of their coordination geometry, which is rather uncommon for Ln(III) ions. In this respect, more promising are lanthanide complexes with forced PBP coordination, which is provided by planar pentadentate chelating ligands in the equatorial plane and two apical ligands. Several PBP lanthanide complexes of this type were synthesized and magnetically characterized in the past years,[22–25] complexes with Kramers lanthanide ions (Dy(III), Er(III)) often behave as SMMs. Recently, Sutter *et al.* reported lanthanide complexes $(Et_3NH)[Ln(H_2DAPS)Cl_2]$ (H_2DAPS = 2,6-diacetylpyridine bis-(salicylhydrazone) and Ln = Tb and Dy) with a distinctly shaped PBP coordination polyhedron produced by the pentagonal N_3O_2 chelate ring of the H_4DAPS ligand in the equatorial plane and two apical chloride ligands.[26] Dynamic magnetic measurements showed that the dysprosium complex is a field-induced SMM with the effective barrier of U_{eff}/k_B = 70 K, while the complex with a non-Kramers Tb(III) ion is SMM-silent. Theoretical analysis for Dy complex based on *ab initio* calculations indicated strongly axial $m_J = \pm 15/2$ ground state of Dy(III) with very small transverse components (g_x, g_y) suppresing the ground-state QTM and resulting in a SMM behavior.[27] Given that PBP lanthanide complexes may display high SMM characteristics, it is of interest to extend the family of $[Ln(H_2DAPS)Cl_2]^-$ complexes to other Ln(III) ions. In particular, it would be informative to compare magnetic behavior of isostructural dysprosium and erbium complexes, especially in view of the fact that Dy(III) and Er(III) ions have the same highest magnetization state ($m_J = \pm 15/2$), but different shape of the electrostatic potential surface (which is oblate for Dy(III) and prolate for Er(III)).[13–18,28] Furthermore, erbium PBP complexes have been only scarcely reported in the literature.[27,29] Following this motivation, here we report the synthesis, crystal structure and magnetic properties of the new erbium PBP complex $(Et_3NH)[Er(H_2DAPS)Cl_2]$ (**1**). In addition to dc and ac magnetic measurements, we also present detailed high-frequency/high-field electron paramagnetic resonance (HF-EPR) spectroscopy investigations which give a deep insight into the magnetic properties of **1**. It is noteworthy that HF-EPR spectroscopy is still rarely applied for Er(III) complexes.[30–33] The reason for this is the often too high zero-field splitting between the lowest and first excided KD as well as highly forbidden transitions within the lowest KD. Among the experimental approaches to gain information on the CF splittings and magnetic anisotropy (optical spectroscopy methods like electron absorption, far-infrared spectroscopy or magnetic circular dichroism measurements[34–39]) HF-EPR spectroscopy is a powerful tool for direct investigation of the CF splitting as well as the magnetic anisotropy. Our experimental studies are supplemented with *ab initio* calculations and CF analysis of the electronic structure of the Er(III) ion, which is based on the simulation of the dc magnetic susceptibility of **1**. Dynamic magnetic measurements indicate that, in contrast to the isostructural Dy(III) complex, **1** reveals no SMM behavior, neither with nor without magnetic field. This feature is discussed in the light of our experimental and theoretical results.

2 Experimental details and methods

The Er(III) mononuclear complex under study with the general formula $(Et_3NH)[Er(H_2DAPS)Cl_2]$ (**1**) was synthesized as following: to a suspension of H_4DAPS (0.46 mmol, 200 mg) in absolute ethanol (20 ml), a solution of $ErCl_3$ in ethanol (0.46 mmol, 126 mg in 10 ml C_2H_5OH) was added at room temperature. The white suspension turned to yellow immediately, and white precipitate started to dissolve. The reaction mixture was refluxed for 1 h under stirring conditions. Subsequently, it cooled down to room temperature and triethylamine (0.14 ml, 1 mmol) was added under stirring. The reaction mixture became more saturated bright yellow after about 5–10 minutes of stirring. Afterwards, the solution was filtered and left for the evaporation of the solvent at room temperature. Crystal formation was observed in 3–5 days under significant evaporation of the solution. The mother liquor was decanted from the crystals, which were washed with diethyl ether and dried in vacuum affording 0.18 g of product **1**. Yield 51%. Anal. Calcd for $C_{29}H_{35}N_6O_4Cl_2Er$ (M.m. 769.8): C, 45.24; H, 4.55; N, 10.92. Found: C, 45.66; H, 4.81; N, 10.93. FT-IR ν_{max}/cm^{-1}: 3166m, 3084m, 1646s, 1640s, 1607m, 1549s, 1493vs, 1453m, 1361m, 1302m, 1230vs, 1163vs, 1083m, 1039m, 990m, 919m, 817vs, 776m.

Single crystal X-ray diffraction measurements of **1** were performed on a Xcalibur diffractometer with EOS CCD detector (Agilent Technologies UK Ltd). Recording of reflections, determination and refinement of unit cell parameters were performed at 100(1) K, with monochromatic MoK_α radiation (0.71073 Å) using the CrysAlis PRO software.[40] The structure was solved by direct methods and refined against all F^2 data. All non-hydrogen atoms were refined with anisotropic thermal parameters. Positions of hydrogen atoms were obtained from difference Fourier syntheses and refined with riding model constraints. Selected crystallographic parameters and the refinement statistics are given in Table 1. The selected bond lengths and angles of **1** are summarized in Table S1.† All calculations were performed with the SHELXTL software suite.[41]

Table 1 Crystal data and structural refinement parameters for **1**

Chemical formula	$C_{29}H_{35}Cl_2ErN_6O_4$
Formula weight	769.79
Cell setting	Orthorhombic
Space group, Z	$Cmc2_1$, 4
Temperature (K)	100(1)
a (Å)	18.7290(5)
b (Å)	14.8702(4)
c (Å)	11.1918(4)
Cell volume (Å^3)	3117.0(2)
ρ (g cm^{-3})	1.640
μ (cm^{-1})	29.08
Crystal size (mm^3)	0.1 × 0.1 × 0.25
Refls collected/unique	5094/3427
R_{int}	0.0327
Θ_{max} (°)	29.06
Parameters refined	212
Final R_1, wR_2 [$I > 2\sigma(I)$]	0.0331, 0.0533
Goodness-of-fit	0.961

The X-ray crystal structure data of **1** have been deposited in the CambridgeCrystallographic Data Center with reference code CCDC 2099114.†

Dc magnetic properties were measured using a MPMS3 Magnetometer (Quantum Design) in the temperature range of T = 1.8–300 K in magnetic fields up to B = 7 T. The sample in the polycrystalline (powder) form was loaded into a gelatine capsule and fixed by eicosane to avoid rearrangements of the crystallites. The experimental data were corrected for the sample holder and the diamagnetic ligand contribution as calculated using Pascal's constants.[42]

Alternating current (ac) measurements were performed using a Physical Properties Measurement System PPMS-9 (Quantum Design) in a 4 Oe oscillating magnetic field with and without an applied static DC field.

High-frequency/high-field electron paramagnetic resonance (HF-EPR) measurements were performed by usage of a millimeter vector network analyser (MVNA) by ABmm as phase sensitive microwave source and detector.[43] The measured spectra were obtained in a frequency range between 80–900 GHz and in external magnetic fields up to 16 T. Temperature control between 2 K and 70 K was ensured by a variable temperature insert (VTI) with He gas flow. The sample was freshly ground and placed inside a brass ring without glue or grease, *i.e.*, as a loose powder sample to allow alignment of the crystallites along their effective anisotropy axis in the external magnetic field. This method has been proven powerful to obtain pseudo-single-crystal spectra with strongly reduced complexity of the observed resonance features, especially for 3d metal containing compounds.[44–50] Due to the finite angle between the two non-equivalently positioned Er(III) molecules within the unit cell it is supposed, that the local anisotropy axis which is assumed to direct perpendicular to the equatorial planes is off the magnetic field direction by about ~22°. While the g-values of the lowest multiplets are deduced from fixed-powder studies, the obtained ZFS parameters do not dependent on the orientation of the molecules with respect to the external magnetic field. Alignment was ensured by applying the maximum field of 16 T prior to the measurements and monitoring the corresponding alignment jumps in the transmitted microwave signal. To avoid rearrangement of the crystallites, the magnetic field range was restricted to 0.2–16 T. To investigate the magnetic anisotropy in various orientations of the crystallites we additionally measured a powder sample which was fixed by eicosan. A commercial DPPH standard was used to approve the external magnetic field strength at the sample position. Spectral simulations were done by using the EasySpin software package.[51]

3 Experimental results

3.1 Crystal structure

Complex **1** crystallizes in the orthorhombic crystal system and space group $Cmc2_1$ and is isostructural to previously reported Dy and Tb analogues.[26] Fig. 1 depicts the molecular structure of the anionic Er(III) complex in **1**.

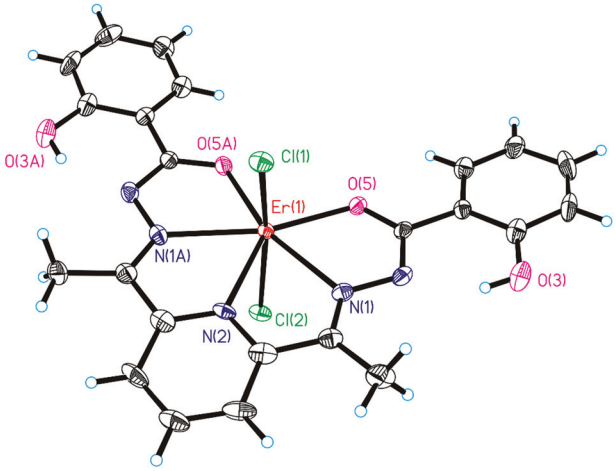

Fig. 1 General view of the anionic complex $[Er(H_2DAPS)Cl_2]^-$ in the crystal structure of **1**.

Donor atoms of the H_2DAPS ligand generate a co-planar equatorial coordination environment of the Er(III) ions with a pseudopentagonal geometry (∠O–Er–N_{im} = 66.5(1)°, ∠N_{py}–Er–N_{im} = 65.54(9)°, and ∠O–Er–O = 96.0(2)°. The equatorial Er–O and Er–N1(N2) bond lengths amount to 2.246(3) and 2.424(4)/2.425(6) Å, respectively. Two Cl^- anions are coordinated at the apical sites with slightly different bond distances of 2.586(2) and 2.654(2) Å and a Cl(1)–Er–Cl(2) bond angle of 166.19(5)°. Continuous-shape-measurement analyses using the SHAPE program[52] reveal a distorted PBP geometry with D_{5h} (pseudo) CF symmetry around the Er(III) ions (see Table S2†).

The crystal packing diagram shown in Fig. S1† reveals two orientations of crystallographically equivalent Er(III)-molecules within the unit cell which are tilted against each other by an angle of approx. 45°. Furthermore it can be seen, that the shortest intermolecular Er–Er distance is ~7.6 Å (Fig. S1†). As previously reported for such type of isostructural complexes,[26] there are essentially no short intermolecular contacts in the crystal structure of **1** which could provide a magnetic superexchange pathway.

3.2 Magnetic susceptibility

The temperature dependence of the magnetic susceptibility for complex **1** was measured under an applied dc magnetic field of 0.1 T in the temperature range of 1.8–300 K as shown in Fig. 2. The χT product at 300 K (11.67(60) cm^3 K mol^{-1}) is close to the expected value of 11.48 cm^3 K mol^{-1} for a free Er(III) ion ($^4I_{15/2}$). Upon cooling down to 100 K, it gradually decreases and then rapidly drops below 100 K as it is characteristic for many lanthanide complexes. The inset in Fig. 2 shows the magnetisation measured at various isothermal conditions in external magnetic fields up to 7 T. In the low field region between 0 and 1 T the magnetisation figures a steep slope. With further increasing external magnetic fields the slope flat-

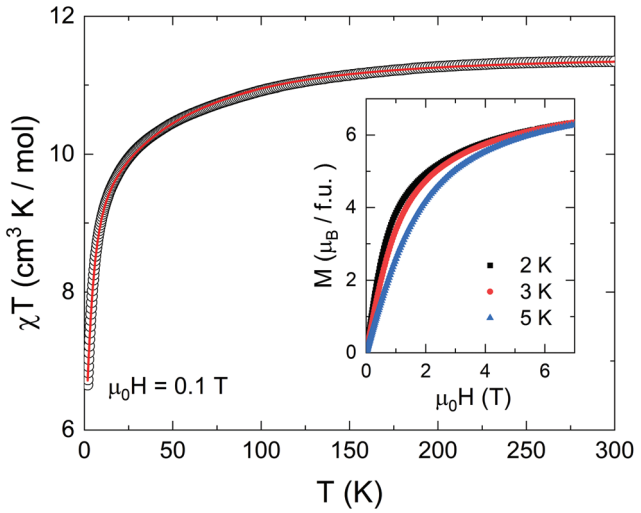

Fig. 2 Experimental (black symbols) and calculated (solid red line) temperature dependence of the χT product for complex **1** measured at $\mu_0 H$ = 0.1 T. Inset: Magnetic field dependence of the dc magnetisation measured at various temperatures as indicated in the plot.

tens to a nearly linear behaviour until the magnetisation reaches its maximum value of 6.36(30)μ_B/f.u. at $\mu_0 H$ = 7 T and 2 K. Within the accessible field range, no saturation of magnetisation is observed.

3.3 Electron paramagnetic resonance

HF-EPR spectra of an oriented loose powder sample **1**, obtained at T = 2 K, display well resolved resonance signals in the whole accessible frequency regime up to 900 GHz (Fig. 3). The resonance features form clear branches (labelled R1 to R3) as indicated by the filled squares and solid lines in the frequency *vs.* magnetic field diagram. In addition to the main resonances, shoulder-like anomalies appearing at the high-field side of the features summarized by R3 are attributed to a small non-perfect alignment of the loose powder as proven by comparative measurements on a fixed powder sample (see Fig. S2†). The main branches feature linear behaviour except for the crossing regime of R1 and R2 which implies an avoided crossing behavior, *i.e.*, it indicates mixing of states.[53] While branch R1 appears to be gapless, the branches R2 and R3 figure a zero-field splitting (ZFS) gap Δ_1 of around 300 GHz.

The temperature dependence of the resonance spectra obtained at measurement frequencies both below and above the ZFS gap (Fig. 4) demonstrates that the resonance features R1 to R3 are associated with ground state transitions. At both frequencies, the features which are observable at T = 2 K (black squares) become weaker in intensity as the temperature rises. In addition, the spectra imply the presence of excited states (ES) which get thermally populated. This is evidenced by the appearance of several additional features indicated by blue and red symbols in Fig. 4. The excited features again obey a linear dependence of the resonance frequencies on the magnetic fields as shown in Fig. 5a (for the measured HF-EPR

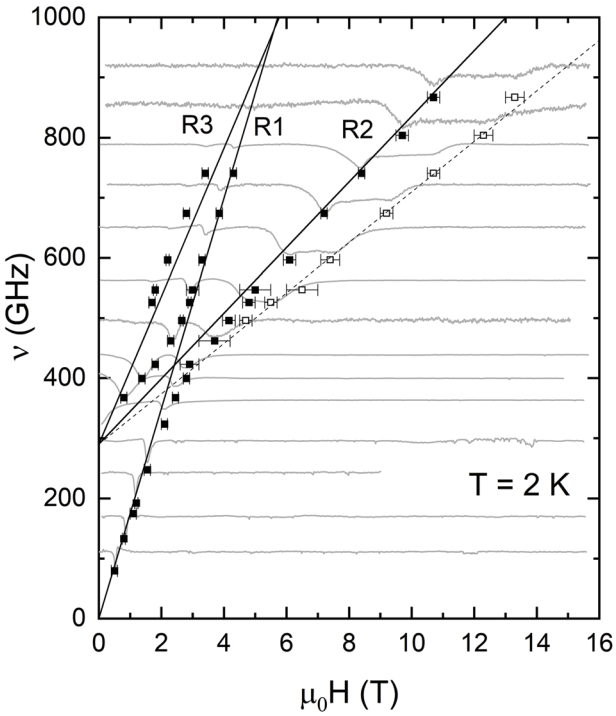

Fig. 3 Frequency *vs.* magnetic field diagram obtained at T = 2 K. Filled squares correspond to the resonance positions of the observed features which form the branches R1–R3 as indicated by the solid lines. Open squares mark a resonance shoulder originating from not perfectly aligned powder. The measured HF-EPR spectra are plotted as grey lines in the background and are vertically shifted in correspondence of the respective resonance positions.

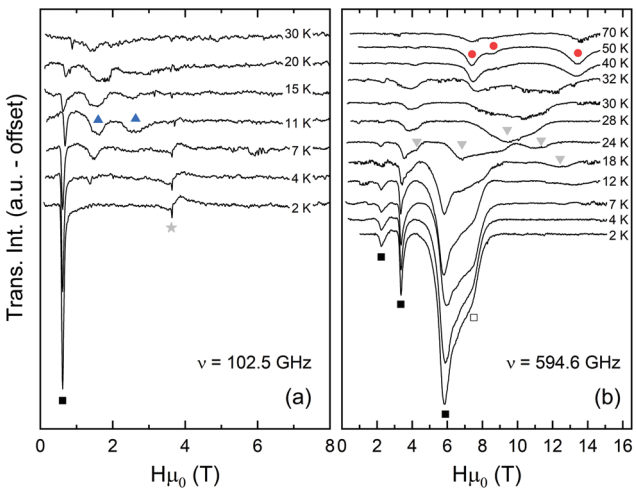

Fig. 4 HF-EPR spectra measured at different fixed temperatures at (a) ν = 102.5 GHz and (b) 594.6 GHz. The symbols mark different resonance features which appear at T = 2 K (black squares), T = 10 K (blue triangles) and T = 50 K (red circles) in correspondence to the branches shown in Fig. 5. Grey triangles in (b) mark features which could not be followed in a frequency-dependent measurement. The grey asterisk in (a) indicates the DPPH marker.

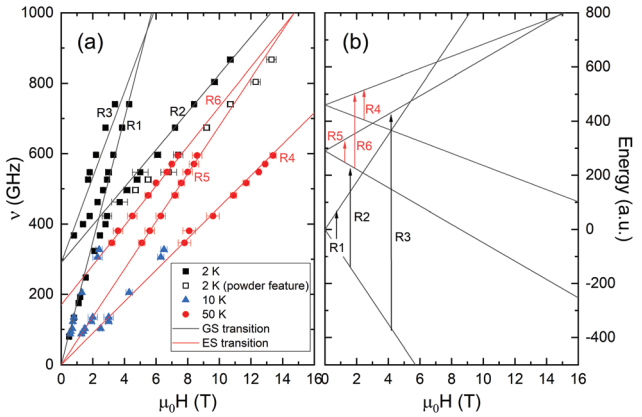

Fig. 5 (a) Frequency *vs.* magnetic field diagram with resonances obtained at different temperatures. Solid black and red lines show simulated ground state (GS) and excited state (ES) transitions corresponding to the arrows in (b) which follow the same color scheme. (b) Modeled energy-level diagram of the energetically lowest three KDs. The arrows mark transitions between the energy-levels for all the observed branches, respectively.

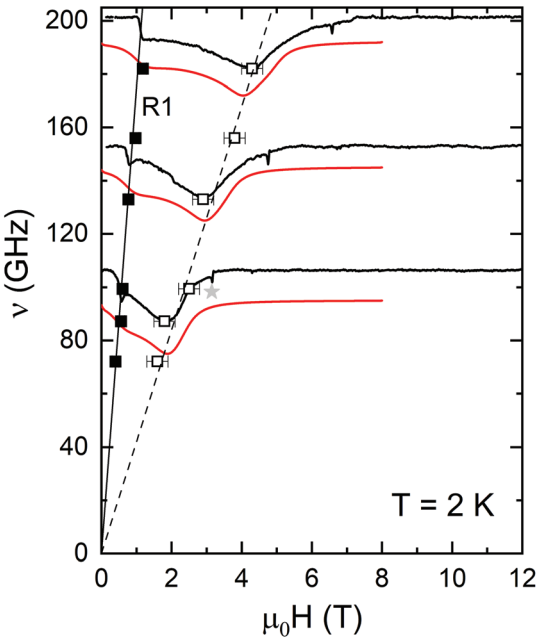

Fig. 6 Frequency *vs.* magnetic field diagram obtained at T = 2 K for a fixed powder sample. Filled and open squares mark positions of the obtained resonance features. Solid and dashed straight lines show a linear fit of the resonance positions. Measured and simulated HF-EPR spectra are plotted as black and red lines, respectively, and are vertically shifted for comparison with the corresponding resonance position. The grey asterisk marks the DPPH signal.

spectra at T = 10 K and 50 K see Fig. S3†). In contrast, the spectra did not allow to study the frequency dependence of the broad resonances marked by grey triangles in Fig. 4b. These features are rather weak and only visible in a narrow temperature range so that they can be hardly discriminated. We attribute their origin to thermal population of excited doublets due to mixing of states which is not covered by the model presented below.

All obtained resonance branches measured at different temperatures on an oriented loose powder sample are summarized in Fig. 5a. The branches R1, R5 and R4 show no ZFS gap which allows us to assign them to transitions within the lowest (KD1), first (KD2) and second (KD3) excited KD, respectively, according to their appearance upon heating as shown in Fig. 4a. From the slope of these branches effective g-values, g_{eff}, of 12.50(40), 4.85(20) and 3.20(20) can be assigned for KD1, KD2 and KD3, respectively.‡ The branches R2, R3 and R6 figure finite ZFS gaps of Δ_1 = 290 GHz for R2 and R3 and Δ_2 = 170 GHz for R6 as well as g_{eff} = 3.9(3), 8.8(3) and 4.5(2), respectively.

These results, *i.e.*, the effective g-values of the ground state and excited KDs as well as the observed ZFS gaps, enable to construct a phenomenological energy-level diagram using a S = 1/2 pseudo-spin approximation for each KD as shown in Fig. 5b.[32,54] The arrows in Fig. 5b assign the observed branches to the transitions from the ground state (black) or excited states (red), respectively. While the construction of this energy-level diagram is exclusively based on the effective g-values observed for the branches R1, R5 and R4 as well as the ZFS gaps Δ_1 and Δ_2, the consistency of the used model is conclusively demonstrated by the observed effective g-values of the branches R2, R3 and R6 which perfectly agree to a transition between the observed KDs as can be seen from the comparison of the measured data with the respective simulated branches shown as solid lines in Fig. 5a.

To further investigate the anisotropy of the lowest lying KD we obtained HF-EPR spectra on a fixed powder sample at T = 2 K. The spectra shown as black solid lines in Fig. 6 figure a typical shape for an axial g-anisotropy.[55] Thus, two distinct resonance positions can be read off, which are marked by filled and open black squares in Fig. 6, respectively. From this, the components of the anisotropic effective g-value of the lowest KD are determined as $g_{\mathrm{eff},z}$ = 12.5(1) and $g_{\mathrm{eff},x/y}$ = 2.9(2).

The red solid lines in Fig. 6 show a spectral simulation using a S = 1/2 pseudo-spin approximation. By comparing the measured data with this simulations we observe a small rhombicity of the g-anisotropy which is not visible by the eye in the individual spectra due to the spectral line broadening. The best simulation parameters are determined to be $g_{\mathrm{eff},z}$ = 12.5(1), $g_{\mathrm{eff},x}$ = 2.6(3) and $g_{\mathrm{eff},y}$ = 3.2(3). All experimentally obtained parameters from the investigation of the aligned loose and fixed powder are summarized in Table 2.

The x, y and z components of the anisotropic effective g-factor from the fixed-powder spectra can be related to the g'_{eff}-factor from the pseudo-single-crystal loose powder spectra, where the effective anisotropy axis of the complex is aligned

‡Note, that due to the alignment of the crystallites, only the effective g-value component which is oriented parallel to the external magnetic field direction can be assigned here.

Table 2 Effective g-values and ZFS gaps obtained from analysing the HF-EPR data by means of a S = 1/2 pseudo-spin approximation for the lowest three KDs. Δ_1 and Δ_2 are the ZFS gaps separating KD1 and KD2 as well as KD2 and KD3, respectively

	g_{eff}	$g_{\mathrm{eff},x,y,z}$	ZFS
KD1	12.5(40)	2.6(3), 3.2(3), 12.5(1)	Δ_1 = 290 GHz
KD2	4.85(20)		Δ_2 = 170 GHz
KD3	3.20(20)		

along the magnetic field direction, *via* the following projection relation:

$$g'^2_{\mathrm{eff}} = g_{\mathrm{eff},z}{}^2 \cos^2(\theta) + g_{\mathrm{eff},x(y)}{}^2 \sin^2(\theta) \quad (1)$$

Here, θ is the angle between the $g_{\mathrm{eff},z}$ main anisotropy axis and the external magnetic field. Since there is a finite angle between the two non-equivalent molecules in the unit cell it is supposed that the local anisotropy axes of Er(III) can be off the magnetic field direction. In a simple approximation, one may assume that the anisotropy axes are perpendicular to the equatorial planes, *i.e.*, pointing along the Cl–Er(III)–Cl axes, which would imply an angle of about 45° between both of them and the effective anisotropy axis in between so that θ = 22.5°. Using eqn (1), this yields $g'_{\mathrm{eff}} \approx 11.6(1)$ which differs from the loose powder result (see Table 2).§ We conclude that the local anisotropy axes are not perfectly perpendicular to the equatorial planes but θ is significantly smaller and close to zero. The packing diagram (see Fig. 7 and Fig. S1(a)†) shows that changes of the relative angle β between the anisotropy axis of a molecule and its equatorial plane may compensate the structural tilting and result in the approximately parallel alignment of the molecular anisotropy axes. A similar tilting angle of about 20° between the anisotropy and the molecular symmetry axis was found for a Dy(III) monomer figuring a PBP surrounding, which supports the presented implications.[29]

3.4 AC Magnetic susceptibility

To investigate the dynamic magnetic behaviour of **1**, the dynamic (ac) susceptibility was measured in a frequency range of 10 Hz–10 kHz for temperatures between 2 K–4 K in zero and non-zero applied dc magnetic field as can be seen in Fig. S4 and S5.† The in-phase $\chi'(\nu)$ and out-of-phase $\chi''(\nu)$ components of the ac susceptibility signal figure no frequency dependence and by this no slow magnetic relaxation behavior was observed with and without applied dc magnetic field, in contrast to the isostructural Dy(III) complex.[26]

4 Crystal field analysis

4.1 Crystal field calculations

In order to relate the magnetic properties and results obtained by HF-EPR measurements on the erbium complex **1** to its electronic structure, we perform a crystal field (CF) analysis of the Er(III) ion. For this, we simulate the dc magnetic properties (see Fig. 2) in the framework of the CF theory for 4f electrons, which is based on the CF Hamiltonian H composed of the free-ion part H_0 and the CF term H_{CF},

$$H = H_0 + H_{\mathrm{CF}}. \quad (2)$$

The free-ion Hamiltonian H_0 comprises atomic interactions of 4f-electrons

$$H_0 = \sum_{k=2,4,6} f_k F^k + \xi_{4\mathrm{f}} \sum_i l_i s_i + \alpha L(L+1) + \beta G(R_7) + \gamma G(G_2) \quad (3)$$

where f_k and F_k are the angular and radial Slater parameters, respectively, the second term is the spin–orbit operator, and α, β, and γ are Trees parameters describing two-electron correlation corrections to the Coulomb repulsion term.[56–58] The H_{CF} Hamiltonian incorporates metal–ligand interactions in the frame of the Wybourne CF parametrization scheme

$$H_{\mathrm{CF}} = \sum_{k,q} B_{kq} C_q^k \quad (4)$$

where B_{kq} are CF parameters (k = 2,4,6; $q \leq k$) and C_q^k are spherical tensor operators for f-electrons.[56–58] The set of B_{kq} parameters specifies the CF potential acting on the 4f-electrons. The B_{kq} quantities are usually treated as adjustable parameters, which are fitted to the optical or magnetic data for lanthanide compounds. Details of CF calculations for Ln(III) ions have been well documented in the literature.[56–58]

The magnetic behavior of lanthanide complexes is simulated in terms of the electronic structure of Ln(III) ions obtained from CF calculations (eqn (2)–(4)). The magnetization M and applied magnetic field H are related by $M = \chi H$, where

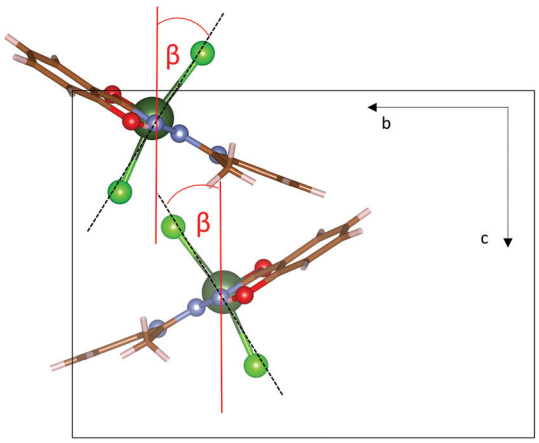

Fig. 7 Part of the packing diagram (see Fig. S1(a)†) showing two non-equivalent molecules. The black box shows the unit cell. The pentagonal planes of the molecules are tilted by ≈ 45° with respect to each other. The angle β indicates tilting of the molecular anisotropy axis from the perpendicular direction.

§ Here, we use $g_{\mathrm{eff},x(y)} = 1/2(g_{\mathrm{eff},x} + g_{\mathrm{eff},y})$.

χ is the tensor of magnetic susceptibility, which is represented by a 3 × 3 matrix $\chi_{\alpha\beta}$,

$$M_\alpha = \sum_\beta \chi_{\alpha\beta} H_\beta \quad (5)$$

where $\alpha, \beta = x, y$ or z (note that M and H are not generally collinear). The matrix elements $\chi_{\alpha\beta}$ of the χ tensor are expressed *via* the wave functions $|i\rangle$ and energies E_i of the CF states of the Hamiltonian in eqn (2) using the Gerloch–McMeeking equation,[59]

$$\chi_{\alpha\beta} = \frac{N_a}{\sum_i \exp\left(\frac{-E_i}{kT}\right)} \times \sum_i \left\{ \sum_j \frac{\langle i|\mu_\alpha|j\rangle\langle j|\mu_\beta|i\rangle}{kT} - \sum_{j\neq i} \frac{\langle i|\mu_\alpha|j\rangle\langle j|\mu_\beta|i\rangle + \langle i|\mu_\beta|j\rangle\langle j|\mu_\alpha|i\rangle}{E_i - E_j} \right\} \exp\left(\frac{-E_i}{kT}\right) \quad (6)$$

where N_A is the Avogadro number, E_i is the energy of the CF state $|i\rangle$, k is the Boltzmann constant, T is the absolute temperature, and μ_α, μ_β are the components of the operator of the magnetic momentum

$$\mu = -\mu_B(L + 2S) \quad (7)$$

where L and S are, respectively, the operators of the total orbital momentum and spin and μ_B is the Bohr magneton. The eigenvalues of the 3 × 3 matrix $\chi_{\alpha\beta}$ (eqn (6)) correspond to the principal components of the anisotropic magnetic susceptibility (χ_x, χ_y and χ_z) and the powder magnetic susceptibility is given by $\chi = (\chi_x + \chi_y + \chi_z)/3$. Eqn (2)–(7) can be used to calculate the CF splitting energies of the $^4I_{15/2}$ multiplet of the Er(III) ion in **1** and to simulate the dc magnetic susceptibility (see Fig. 2). In these calculations, the CF parameters B_{kq} are obtained from the fitting of the simulated χT curve to the experimental dc magnetic data (see Fig. 2). CF calculations based on the fitting to the dc magnetic susceptibility can be quite successful for lanthanide compounds containing metal centers with a high enough symmetry, when the number of variables is not too large (about 10 or less) to avoid overparameterization. In particular, such calculations have been performed for erbium compounds Er(trensal)[30] and Er(trenovan)[31] containing Er centers with the C_3 symmetry. However, this CF computational scheme cannot directly be applied to the low-symmetry lanthanide complex **1** because the fitting to the χT curve (Fig. 2) is heavily over-parameterized due to large number of B_{kq} parameters (namely, as many as $27 B_{kq}$ parameters for the C_1 point symmetry of the Er(III) ion in **1**). To overcome this issue, we take advantage of the superposition CF model[60–62] which expresses the B_{kq} parameters *via* the geometry of the metal site in terms of intrinsic CF parameters $b_k(R_0)$ describing local metal–ligand interactions,

$$B_{kq} = \sum_n b_k(R_0)\left(\frac{R_0}{R_n}\right)^{t_k} C_q^k(\theta_n, \phi_n) \quad (8)$$

where the index n runs over metal–ligand pairs involved in the coordination polyhedron of the Ln(III) ion, $b_k(R_0)$ are the three (k = 2, 4, 6) intrinsic CF parameters, (R_n, θ_n, φ_n) are polar coordinates of the n-th ligand atom, t^k are power-law exponents and R_0 is the reference distance (which is normally set to the average metal–ligand distance). The superposition CF model as well as its foundation and applications for f-block element compounds have been described in the literature.[60,62]

In the frame of this approach, the B_{kq} parameters are determined from the fitting to the experimental χT curves of complex **1** (Fig. 2). Intrinsic CF parameters $b_k(R_0)$ vary independently for the O, N and Cl coordinating atoms. The reference distances correspond to average metal–ligand distances (R_0(O) = 2.25 Å, R_0(N) = 2.42 Å and R_0(Cl) = 2.60 Å) and the power-law indexes are fixed at $t^2 = 5$, $t^4 = 8$, and $t^6 = 11$.[60–62] The polar coordinates (R_n, θ_n, φ_n) in eqn (8) describe atomic positions of the O, N and Cl atoms of the $ErN_3O_3Cl_2$ coordination polyhedrons in **1**. These coordinates are taken from the actual crystallographic data for the erbium complex **1**. Atomic parameters of the Er(III) ion (F^2, F^4, F^6, ξ_{4f}, α, β, and γ) involved in the free-ion Hamiltonian H_0 (eqn (3)) are taken from ref. 63.

The second-order contributions from the excited CF states $|i\rangle$ to the $\chi_{\alpha\beta}$ tensor of the magnetic susceptibility (the second term in eqn (6)) involve both the ground J-multiplet ($^4I_{15/2}$) and several excited multiplets of the Er(III) ion ($^4I_{13/2}$, $^4I_{11/2}$, $^4I_{9/2}$). To attain the best agreement with the experimental dc magnetic data, especially at low temperatures, we apply refined CF calculations, in which the rank two (k = 2) B_{kq} parameters are varied instead of the b_2 'intrinsic' CF parameter. The reason is that the second rank CF parameters are sensitive to the long-range interactions, whose range is beyond the $ErN_3O_2Cl_2$ coordination polyhedron. Thus, they are missed in the frame of the superposition CF model. Numerical calculations are carried out with specially designed routines outlined in ref. 64–66.

The best fit to the experimental χT curve for **1** (Fig. 2) is reached at b_4 = 300, b_6 = 279.6 cm^{-1} (for O atoms), b_4 = 262.9, b_6 = 161.0 cm^{-1} (for N) and b_4 = 392.0, b_6 = 199.0 cm^{-1} (for Cl). The calculated rank two B_{2q} parameters are listed in Table S3.† The JM composition of wave function of KD1, KD2 and KD3 is presented in Table S4.† The simulated χT curve for **1** is consistent with the experimental data in the whole temperature range (Fig. 2).

The data indicate that the heteroligand ($N_3O_2Cl_2$) pentagonal bipyramidal coordination of the Er(III) ion in **1** produces a low CF splitting energy of the lowest $^4I_{15/2}$ multiplet (245 cm^{-1}, Table 3). The overall strength of the CF potential is quantified by the CF strength criterion, S = 439.8 cm^{-1}.[67] The most important point is that the CF analysis confirms the presence of two low-lying CF states (Kramers doublets KD2 and KD3) which are seen in the HF-EPR spectra at 290 GHz (9.7 cm^{-1})

and 460 GHz (15.3 cm^{-1}), respectively. The calculated energy position of the first excited CF state KD2 (9.0 cm^{-1}) agrees well with the measured value from the HF-EPR (290 GHz, 9.7 cm^{-1}). The calculated energy of the second excited CF state KD3 (22.0 cm^{-1}) is also reasonably comparable with the HF-EPR data (15.3 cm^{-1}), albeit lying somewhat higher. The calculated *g*-tensor components of the ground CF state KD1 (g_x = 2.07, g_y = 4.88, g_z = 12.37, see Table 3) are fairly close to those obtained from HF-EPR measurements ((g_x = 2.6, g_y = 3.2, g_z = 12.5). Therefore, the CF analysis confirms the axial Ising-type magnetic anisotropy of the ground state KD1 of erbium complex **1**. On the other hand, the calculated *g*-tensor of KD2 is more isotropic (Table 3) and its average value of g_{av} = 5.60 is roughly comparable to g_{eff} = 4.85 estimated from the HF-EPR data for an oriented loose powder sample.

4.2 *Ab initio* calculcations

To asses the electronic structure of the Er(III) ion in compound **1**, we have performed *ab initio* CASSCF/RASSI + SO/SINGLE_ANISO calculation for isolated $[Er(H_2DAPS)Cl_2]^-$ complex using OpenMolcas program.[68,69] All calculations were based on the experimental structure of the $[Er(H_2DAPS)Cl_2]^-$ complex in compounds **1**. The [ANO-RCC...8s7p5d3f2g1h.] basis set for the Er atom, the [ANO-RCC...3s2p1d] for Cl, N and O atoms, [ANO-RCC...3s2p] for C atoms and [ANO-RCC...2s] for H atoms have been employed. The ground state of the $4f^{11}$-electronic configuration of Er(III) is the $^4I_{15/2}$ multiplet. Initially, we have generated the guess orbitals, from which we have selected 7 Er-based starting orbitals occupied by 11 electrons to perform the CASSCF calculations with an active space of CAS (11,7). Using the active space involving 35 quartets and 112 doublets, the configuration interaction (CI) procedure have been computed. After that, all these 35 quartets and all 112 doublets using RASSI-SO module have been mixed to compute the spin–orbit states. The second-order Douglas–Kroll–Hess[70–73] scalar relativistic Hamiltonian was used to treat the scalar relativistic effects. After computing these spin–orbit states, using SINGLE_ANISO code[74] the corresponding *g*-tensors and the CF parameters for the eight low-lying Kramers doublets (KD) have been extracted. The Cholesky decomposition for two electron integrals is employed throughout in the calculations to reduce the disk space.

Table 3 Calculated CF splitting energies of the ground $^4I_{15/2}$ multiplet of the Er(III) ion in **1** and the *g*-tensors of the ground and first excited CF states

CF energies (cm^{-1})	g_x, g_y, g_z
0	2.07, 4.88, 12.37
9.0	2.70, 6.34, 7.75
22	2.14, 5.36, 10.03
74.1	
130.3	
203.7	
207.8	
245.5	

Table 4 The *ab initio* computed CF energies (cm^{-1}) and the *g*-tensors of the ground and two first excited CF states of $Er(H_2DAPS)Cl_2$

CF energies (cm^{-1})	g_x, g_y, g_z
0	0.439, 0.547, 15.040
26.24	7.308, 6.727, 4.135
60.15	4.679, 5.347, 7.072
159.71	
199.31	
281.43	
399.21	
423.48	

Results of *ab initio* calculations for erbium complex **1** are summarized in Table 4, Table S5 and in Fig. S6 and S7.† These data show that CF energies and the ground-state *g*-tensor obtained from *ab initio* calculations (Table 4) differs considerably from those obtained from HF-EPR study (Table 2) and CF calculations (Table 3). The calculated magnetic susceptibility does not reproduce the experimental data (see Fig. S6 ESI†). The overall behavior of the calculated χT curve indicates that *ab initio* calculations overestimate considerably the energy positions of the two first excited CF states KD2 and KD3 (which are responsible for the rapid fall of the χT product at low temperatures) as well as the total energy of the CF splitting of the $^4I_{15/2}$ multiplet. The latter fact can be seen from the lower value of magnetic susceptibility and from the larger slope of the χT curve at room temperature. Therefore, results of *ab initio* CASSCF/RASSI + SO/SINGLE_ANISO calculations for isolated $[Er(H_2DAPS)Cl_2]^-$complex provide a rather approximate insight into the electronic structure of the ground and excited CF states, which cannot be used for a precise comparison with the experimental HF-EPR data and dc magnetic behavior.

5. Discussion and conclusions

Based on the obtained experimental and theoretical results, we discuss the electronic structure and magnetic properties of the prolate Er(III) ion in the heteroligand ($N_3O_2Cl_2$) PBP coordination in comparison to the magnetic characteristics of the oblate Dy(III) ion with the same coordination in the isostructural dysprosium complex $(Et_3NH)[Dy(H_2DAPS)Cl_2]$.[26] Our CF analysis indicates an axial nature of the CF potential of the Er(III) ion in **1**, as evidenced by the fact that the axial CF parameter B_{40} = 1207 cm^{-1} strongly dominates over other CF parameters B_{kq} (< 300 cm^{-1}, Table S3 in ESI†). Calculations indicate that the apical (Cl_2) and equatorial (N_3O_2) ligands in complex$[Er(H_2DAPS)Cl_2]^-$ approximately equally contribute to B_{40}. The dominance of the axial CF parameter B_{40} determines the overall anisotropic magnetic behavior of the Er(III) ion, which is reflected in the Ising-type character of the ground-state *g*-tensor of KD1, as documented from the HF-EPR study (Table 2), CF analysis (Table 3) and *ab initio* calculations (Table 4). Basically, the main characteristics of the Er(III) ion in **1** are reasonably reproduced with the use of the axial CF para-

meter B_{40} only, such as the presence of low-lying CF states (Table S6†) and magnetic susceptibility (especially below 20 K and above 200 K, Fig. S8†). In this limiting case of a strictly axial CF, the ground state is the Ising-type KD with $m_J = \pm 11/2$ ($g_x = g_y = 0$, $g_z = 13.156$) and the low-lying exited CF states are $m_J = \pm 9/2$ (8.2 cm^{-1}), $\pm 7/2$ (49.0 cm^{-1}) and $\pm 13/2$ (53.1 cm^{-1}), Table S6.† The non-axial CF terms B_{kq} arising mainly from the distorted equatorial pentagon N_3O_2 (the largest of which are $B_{44} = -213$, $B_{64} = 156$ and $B_{66} = -284$ cm^{-1}, Table S3†) strongly mix these $\pm M$ states to produce the ground state KD1 (with the wave function $0.57|\pm 9/2\rangle + 0.15|\pm 7/2\rangle + 0.11|\pm 3/2\rangle + \ldots$) and two excited states KD2 (9.7 cm^{-1}) and KD3 (15.3 cm^{-1}), which are observed in the HF-EPR spectra. Upon this mixing the ground state KD1 retains high axiality but loses perfect Ising-type character due to the appearance of a significant transverse components in the g-tensor, such as $g_x = 2.6$, $g_y = 3.2$, $g_z = 12.5$ (from HF-EPR) and $g_x = 2.07$, $g_y = 4.88$, $g_z = 12.37$ (from CF analysis). The important role of the transverse components of the anisotropic g-tensor for the magnetic relaxation mechanisms has been extensively studied in the literature.[75–79] Therefore, the SMM-silent behavior of **1** is straightforwardly explained in terms of our experimental and theoretical results because considerable non-axiality of KD1 causes fast QTM in the ground state resulting in the absence of slow magnetic relaxation. This unfavorable situation is further aggravated by the presence of a low-lying state KD2 (at 9.7 cm^{-1}) with even stronger non-axiality, through which very fast thermally activated TA-QTM can occur. Probalities of QTM, TA-QTM and Orbach relaxation processes involving the KD1 and KD2 states are estimated from *ab initio* calculations for **1** (see Fig. S7†).

Now we apply our results to asses the magnetic behavior of the oblate Dy(III) ion in the same ligand coordination in compound $(Et_3NH)[Dy(H_2DAPS)Cl_2]$.[26] For this, we calculate the CF splitting energies of the ground $^6H_{15/2}$ multiplet and wave functions of the Dy(III) ion using the same set of CF parameters obtained for $[Er(H_2DAPS)Cl_2]^-$ (see Table S3†). The results are presented in Table S7.† They indicate that the Dy(III) ion in the PBP heteroatomic coordination $DyN_3O_2Cl_2$ possesses necessary prerequisites to be a SMM, *i.e.*, the Ising-type nature of the well-isolated ground state, represented by an almost pure wave function $0.989|\pm 15/2\rangle$ and nearly perfect Ising-type g-tensor with $g_z \approx 20$ and very small transverse components g_x and g_y (Table S7†). Therefore, our results are consistent with the observation of SMM behavior for the isostructural complex $[Dy(H_2DAPS)Cl_2]^-$ with $U_{eff}/k_B \approx 70$ K.[26] Qualitatively, these results give some insight into the magnetic relaxation mechanism of the Dy(III) ion, which is seemingly due do suppressed QTM in the ground state $0.989|\pm 15/2\rangle$ ($g_x = 0.034$, $g_y = 0.075$, $g_z = 19.743$) and fast TA-QTM relaxation through the first excited state with dominant component $0.924|\pm 1/2\rangle$ exhibiting strong non-axiality ($g_x = 1.306$, $g_y = 6.856$, $g_z = 13.652$, Table S7†). In this case the energy barrier U_{eff} is controlled by the energy position of the first exited CF state. Similar results for the ground and first excited CF states of Dy(III) have been recently obtained from *ab initio* CASSCF/RASSI + SO/SINGLE_ANISO calculations for the $[Dy(H_2DAPS)Cl_2]^-$ complex, which indicate suppressed QTM in the highly axial ground state $m_J = \pm 15/2$ ($g_x = 0.009$, $g_y = 0.016$, $g_z = 19.741$) and fast TA-QTM through the first excited state ($g_x = 0.454$, $g_y = 1.287$, $g_z = 14.174$, see Table 2 in ref. 27). It is also noteworthy that a SMM performance with a comparable barrier of $U_{eff} = 58$ cm^{-1} have been recently reported for a PBP Dy(III) complex $[Dy(THF)_5Cl_2]^+$ $[BPh_4]^-$ (THF = tetrahydrofuran) with two apical Cl ligands and five THF molecules in the equatorial plane.[80] Considering PBP coordination around Dy(III) with the two apical Cl ligands, it is likely that the magnetic relaxation mechanism follows the same scenario as that in $[Dy(H_2DAPS)Cl_2]^-$.

In the wider context, the difference between the SMM behavior of Er(III) and Dy(III) ions in the isostructural compounds with the same PBP coordination polyhedron $LnN_3O_2Cl_2$ is well consistent with the general concept of magnetic behavior of Ln(III) ions with oblate (Ln = Ce, Pr, Nd, Tb, Dy and Ho) and prolate (Ln = Pm, Sm, Er, Tm and Yb) shape of the electron density distribution of the $4f^n$ shell,[28] namely the dominant axial CF in the $[Ln(H_2DAPS)Cl_2]^-$ complexes (Ln = Dy, Er) induces SMM behavior in the oblate Dy(III) ions and does not in the prolate Er(III) ion. Analogous contrasting SMM behavior of isostructural Dy and Er PBP complexes has been reported in ref. 27.

In conclusion, we have synthesized the mononuclear Er(III) complex $(Et_3NH)[Er(H_2DAPS)Cl_2]$ with a distinct PBP coordination provided by the planar pentadentate ligand H_2DAPS in the equatorial plane and two apical chloride ligands. The sample has been fully characterized structurally and magnetically. We report detailed spectroscopic HF-EPR investigations for this complex, from which we were able to precisely determine the CF splittings ($\Delta_1 = 290$ GHz and $\Delta_2 = 170$ GHz) between the lowest three KDs of the Er(III) ion. Furthermore, we measured the effective g-value for the transitions within these KDs as well as the g-anisotropy of the ground KD. We also performed *ab initio* CASSCF/RASSI + SO/SINGLE_ANISO calculation for isolated $[Er(H_2DAPS)Cl_2]^-$ complex and provided CF analysis of the energy splitting pattern of the lowest $^4I_{15/2}$ multiplet of Er(III) ion in a distorted (low-symmetry) hetero-ligand PBP coordination ($N_3O_2Cl_2$), which is based on the simulation of the dc magnetic data. The results of the CF calculations of energy positions for the three lowest KDs and their anisotropic g-tensors are well consistent with the experimental HF-EPR results, especially for the ground-state KD1. The absence of the SMM behavior in $(Et_3NH)[Er(H_2DAPS)Cl_2]$ complex established from ac magnetic measurements can be attributed to a pronounced non-axiality of the ground-state g-tensor ($g_x = 2.6$, $g_y = 3.2$, $g_z = 12.5$) promoting a fast QTM magnetic relaxation. The origin of the contrasting SMM properties of isostructural Er(III) and Dy(III) PBP complexes has been analyzed in terms of our experimental and theoretical results.

Author contributions

Conceptualization: R. K., V. S. M., and E. B. Y.; HF-EPR and DC magnetometry experiments: L. S.; HF-EPR analysis: L. S., Ch.

K., and R. K.; synthesis and characterization: V. A. K.; X-ray crystallography: D. V. K.; AC magnetometry experiments: O. V. M. and A. N. V.; DC magnetometry analysis and theoretical calculations, V. S. M. and D. V. K.; writing–original draft preparation: L. S., R. K., V. S. M., D. V. K.; writing–review and editing: L. S., R. K., V. S. M. and E. B. Y; supervision, project administration: R. K., A.N.V. and E.B.Y.

Conflicts of interest

There are no conflicts to declare.

Acknowledgements

We acknowledge financial support by BMBF *via* the project SpinFun (13XP5088) and by Deutsche Forschungsgemeinschaft (DFG) under Germany's Excellence Strategy EXC2181/1-390900948 (the Heidelberg STRUCTURES Excellence Cluster). Support by the Ministry of Education and Science of the Russian Federation within the framework of the governmental program of Megagrants 075-15-2021-604 is acknowledged. C. K. acknowledges support by the DFG *via* project KO 5480/1-1. Acknowledgments: V. S. M., V. A. K., and E. B. Y. are grateful for the financial support from the Russian Science Foundation (RSF project no. 18-13-00264) in part of synthesis, calculations of the electronic structure and theoretical analysis of dc magnetic properties. X-ray diffraction analysis has been supported by the IPCP RAS state assignment (no. AAAA-A19-119092390076-7).

Notes and references

1 M. N. Leuenberger and D. Loss, *Nature*, 2001, **410**, 789–793.
2 L. Bogani and W. Wernsdorfer, *Molecular spintronics using single-molecule magnets*, Nanoscience and Technology, Co-Published with Macmillan Publishers Ltd, UK, 2009.
3 M. Mannini, F. Pineider, P. Sainctavit, C. Danieli, E. Otero, C. Sciancalepore, A. M. Talarico, M.-A. Arrio, A. Cornia, D. Gatteschi and R. Sessoli, *Nat. Mater.*, 2009, **8**, 194–197.
4 P. C. E. Stamp and A. Gaita-Ariño, *J. Mater. Chem.*, 2009, **19**, 1718–1730.
5 A. Ardavan and S. J. Blundell, *J. Mater. Chem.*, 2009, **19**, 1754–1760.
6 M. Affronte, *J. Mater. Chem.*, 2009, **19**, 1731–1737.
7 S. Sanvito, *Chem. Soc. Rev.*, 2011, **40**, 3336–3355.
8 F. Troiani and M. Affronte, *Chem. Soc. Rev.*, 2011, **40**, 3119–3129.
9 E. Moreno-Pineda, C. Godfrin, F. Balestro, W. Wernsdorfer and M. Ruben, *Chem. Soc. Rev.*, 2018, **47**, 501–513.
10 R. Sessoli, D. Gatteschi, A. Caneschi and M. A. Novak, *Nature*, 1993, **365**, 141–143.
11 D. Gatteschi, R. Sessoli and J. Villain, *Molecular nanomagnets*, Oxford University Press, Oxford, New York, 2006.
12 N. Ishikawa, M. Sugita, T. Ishikawa, S.-y. Koshihara and Y. Kaizu, *J. Am. Chem. Soc.*, 2003, **125**, 8694–8695.
13 R. Sessoli and A. K. Powell, *Coord. Chem. Rev.*, 2009, **253**, 2328–2341.
14 D. N. Woodruff, R. E. P. Winpenny and R. A. Layfield, *Chem. Rev.*, 2013, **113**, 5110–5148.
15 J. Tang and P. Zhang, *Lanthanide Single Molecule Magnets*, Springer Berlin Heidelberg, Berlin, Heidelberg, 2015.
16 *Lanthanides and actinides in molecular magnetism*, ed. R. A. Layfield and M. Murugesu, Wiley-VCH-Verl, Weinheim, 2015.
17 C. Benelli and D. Gatteschi, *Introduction to molecular magnetism: from transition metals to lanthanides*, Wiley-VCH, Weinheim, 2015.
18 F. Habib and M. Murugesu, *Chem. Soc. Rev.*, 2013, **42**, 3278–3288.
19 C. A. P. Goodwin, F. Ortu, D. Reta, N. F. Chilton and D. P. Mills, *Nature*, 2017, **548**, 439–442.
20 F.-S. Guo, B. M. Day, Y.-C. Chen, M.-L. Tong, A. Mansikkamäki and R. A. Layfield, *Science*, 2018, **362**, 1400–1403.
21 Y.-S. Ding, N. F. Chilton, R. E. P. Winpenny and Y.-Z. Zheng, *Angew. Chem., Int. Ed.*, 2016, **55**, 16071–16074.
22 E. L. Gavey and M. Pilkington, *Polyhedron*, 2016, **108**, 122–130.
23 E. L. Gavey, Y. Beldjoudi, J. M. Rawson, T. C. Stamatatos and M. Pilkington, *Chem. Commun.*, 2014, **50**, 3741–3743.
24 V. D. Sasnovskaya, V. A. Kopotkov, A. V. Kazakova, A. D. Talantsev, R. B. Morgunov, S. V. Simonov, L. V. Zorina, V. S. Mironov and E. B. Yagubskii, *New J. Chem.*, 2018, **42**, 14883–14893.
25 T. A. Bazhenova, V. S. Mironov, I. A. Yakushev, R. D. Svetogorov, O. V. Maximova, Y. V. Manakin, A. B. Kornev, A. N. Vasiliev and E. B. Yagubskii, *Inorg. Chem.*, 2020, **59**, 563–578.
26 A. K. Bar, P. Kalita, J.-P. Sutter and V. Chandrasekhar, *Inorg. Chem.*, 2018, **57**, 2398–2401.
27 P. Kalita, N. Ahmed, A. K. Bar, S. Dey, A. Jana, G. Rajaraman, J.-P. Sutter and V. Chandrasekhar, *Inorg. Chem.*, 2020, **59**, 6603–6612.
28 J. D. Rinehart and J. R. Long, *Chem. Sci.*, 2011, **2**, 2078–2085.
29 S. K. Gupta, T. Rajeshkumar, G. Rajaraman and R. Murugavel, *Chem. Sci.*, 2016, **7**, 5181–5191.
30 E. Lucaccini, L. Sorace, M. Perfetti, J.-P. Costes and R. Sessoli, *Chem. Commun.*, 2014, **50**, 1648–1651.
31 E. Lucaccini, J. J. Baldoví, L. Chelazzi, A.-L. Barra, F. Grepioni, J.-P. Costes and L. Sorace, *Inorg. Chem.*, 2017, **56**, 4728–4738.
32 J. Li, M. Kong, L. Yin, J. Zhang, F. Yu, Z.-W. Ouyang, Z. Wang, Y.-Q. Zhang and Y. Song, *Inorg. Chem.*, 2019, **58**, 14440–14448.
33 M. J. Giansiracusa, E. Moreno-Pineda, R. Hussain, R. Marx, M. Martínez Prada, P. Neugebauer, S. Al-Badran, D. Collison, F. Tuna, J. van Slageren, S. Carretta, T. Guidi, E. J. L. McInnes, R. E. P. Winpenny and N. F. Chilton, *J. Am. Chem. Soc.*, 2018, **140**, 2504–2513.

34 P. Cieslik, P. Comba, W. Hergett, R. Klingeler, G. F. P. Plny, L. Spillecke and G. Velmurugan, *Z. Anorg. Allg. Chem.*, 2021, **647**, 843–849.
35 R. Marx, F. Moro, M. Dörfel, L. Ungur, M. Waters, S. D. Jiang, M. Orlita, J. Taylor, W. Frey, L. F. Chibotaru and J. van Slageren, *Chem. Sci.*, 2014, **5**, 3287–3293.
36 Y. Rechkemmer, J. E. Fischer, R. Marx, M. Dörfel, P. Neugebauer, S. Horvath, M. Gysler, T. Brock-Nannestad, W. Frey, M. F. Reid and J. van Slageren, *J. Am. Chem. Soc.*, 2015, **137**, 13114–13120.
37 G. Cucinotta, M. Perfetti, J. Luzon, M. Etienne, P.-E. Car, A. Caneschi, G. Calvez, K. Bernot and R. Sessoli, *Angew. Chem., Int. Ed.*, 2012, **51**, 1606–1610.
38 P. Comba, L. J. Daumann, R. Klingeler, C. Koo, M. J. Riley, A. E. Roberts, H. Wadepohl and J. Werner, *Chem. – Eur. J.*, 2018, **24**, 5319–5330.
39 E. Moreno Pineda, N. F. Chilton, R. Marx, M. Dörfel, D. O. Sells, P. Neugebauer, S.-D. Jiang, D. Collison, J. van Slageren, E. J. McInnes and R. E. Winpenny, *Nat. Commun.*, 2014, **5**, 5243.
40 CrysAlis PRO version 171.36.20, Agilent Technologies UK Ltd, Yarnton, Oxfordshire, England, 2012.
41 G. M. Sheldrick, *Acta Crystallogr.*, 2015, **A71**, 3–8.
42 G. A. Bain and J. F. Berry, *J. Chem. Educ.*, 2008, **85**, 532.
43 P. Comba, M. Großhauser, R. Klingeler, C. Koo, Y. Lan, D. Müller, J. Park, A. Powell, M. J. Riley and H. Wadepohl, *Inorg. Chem.*, 2015, **54**, 11247–11258.
44 A.-L. Barra, L.-C. Brunel, D. Gatteschi, L. Pardi and R. Sessoli, *Acc. Chem. Res.*, 1998, **31**, 460–466.
45 A. L. Barra, A. Caneschi, D. Gatteschi and R. Sessoli, *J. Am. Chem. Soc.*, 1995, **117**, 8855–8856.
46 D. P. Goldberg, J. Telser, J. Krzystek, A. G. Montalban, L.-C. Brunel, A. G. M. Barrett and B. M. Hoffman, *J. Am. Chem. Soc.*, 1997, **119**, 8722–8723.
47 S. M. J. Aubin, Z. Sun, L. Pardi, J. Krzystek, K. Folting, L.-C. Brunel, A. L. Rheingold, G. Christou and D. N. Hendrickson, *Inorg. Chem.*, 1999, **38**, 5329–5340.
48 S. M. J. Aubin, N. R. Dilley, L. Pardi, J. Krzystek, M. W. Wemple, L.-C. Brunel, M. B. Maple, G. Christou and D. N. Hendrickson, *J. Am. Chem. Soc.*, 1998, **120**, 4991–5004.
49 Y. Krupskaya, A. Alfonsov, A. Parameswaran, V. Kataev, R. Klingeler, G. Steinfeld, N. Beyer, M. Gressenbuch, B. Kersting and B. Büchner, *ChemPhysChem*, 2010, 1961–1970.
50 L. Spillecke, S. Tripathi, C. Koo, M. Ansari, S. Vaidya, A. Rasamsetty, T. Mallah, G. Rajaraman, M. Shanmugam and R. Klingeler, *Polyhedron*, 2021, **208**, 115389.
51 S. Stoll and A. Schweiger, *J. Magn. Reson.*, 2006, **178**, 42–55.
52 M. Llunell, D. Casanova, J. Cirera, P. Alemany and S. Alvares, *SHAPE: Program for the Stereochemical Analysis of Molecular Fragments by Means of Continuous Shape Measures and Associated Tools*, 2013.
53 R. Rakhimov, H. Horton, D. Jones, G. Loutts and H. Ries, *Chem. Phys. Lett.*, 2000, **319**, 639–644.
54 A. Abragam and B. Bleaney, *Electron paramagnetic resonance of transition ions*, Oxford University Press, Oxford, 2012.
55 W. R. Hagen, *Dalton Trans.*, 2006, 4415–4434.
56 B. G. Wyborne, *Spectroscopic Properties of Rare Earths*, Interscience, New York, 1965.
57 S. Hüfner, *Optical spectra of transparent rare earth compounds*, Academic Press, New York, 1978.
58 L. Eyring and K. A. Gschneidner, *Handbook on the physics and chemistry of rare earths*, 1999.
59 M. Gerloch and R. F. McMeeking, *J. Chem. Soc., Dalton Trans.*, 1975, 2443.
60 D. J. Newman and B. Ng, *Rep. Prog. Phys.*, 1989, **52**, 699–762.
61 C. Bungenstock, T. Tröster and W. B. Holzapfel, *Phys. Rev. B: Condens. Matter Mater. Phys.*, 2000, **62**, 7945–7955.
62 D. J. Newman, *Aust. J. Phys.*, 1978, **31**, 79–93.
63 W. T. Carnall, P. R. Fields and K. Rajnak, *J. Chem. Phys.*, 1968, **49**, 4412–4423.
64 V. S. Mironov and L. E. Li, *J. Alloys Compd.*, 1998, **279**, 83–92.
65 V. S. Mironov, Y. G. Galyametdinov, A. Ceulemans and K. Binnemans, *J. Chem. Phys.*, 2000, **113**, 10293–10303.
66 V. S. Mironov, Y. G. Galyametdinov, A. Ceulemans, C. Görller-Walrand and K. Binnemans, *J. Chem. Phys.*, 2002, **116**, 4673–4685.
67 R. P. Leavitt, J. B. Gruber, N. C. Chang and C. A. Morrison, *J. Chem. Phys.*, 1982, **76**, 4775–4788.
68 I. F. Galván, M. Vacher, A. Alavi, C. Angeli, F. Aquilante, J. Autschbach, J. J. Bao, S. I. Bokarev, N. A. Bogdanov, R. K. Carlson, L. F. Chibotaru, J. Creutzberg, N. Dattani, M. G. Delcey, S. S. Dong, A. Dreuw, L. Freitag, L. M. Frutos, L. Gagliardi, F. Gendron, A. Giussani, L. González, G. Grell, M. Guo, C. E. Hoyer, M. Johansson, S. Keller, S. Knecht, G. Kovačević, E. Källman, G. Li Manni, M. Lundberg, Y. Ma, S. Mai, J. P. Malhado, P. A. Malmqvist, P. Marquetand, S. A. Mewes, J. Norell, M. Olivucci, M. Oppel, Q. M. Phung, K. Pierloot, F. Plasser, M. Reiher, A. M. Sand, I. Schapiro, P. Sharma, C. J. Stein, L. K. Sørensen, D. G. Truhlar, M. Ugandi, L. Ungur, A. Valentini, S. Vancoillie, V. Veryazov, O. Weser, T. A. Wesołowski, P.-O. Widmark, S. Wouters, A. Zech, J. P. Zobel and R. Lindh, *J. Chem. Theor. Comput.*, 2019, **15**, 5925–5964.
69 F. Aquilante, J. Autschbach, A. Baiardi, S. Battaglia, V. A. Borin, L. F. Chibotaru, I. Conti, L. De Vico, M. Delcey, I. F. Galván, N. Ferré, L. Freitag, M. Garavelli, X. Gong, S. Knecht, E. D. Larsson, R. Lindh, M. Lundberg, P. A. Malmqvist, A. Nenov, J. Norell, M. Odelius, M. Olivucci, T. B. Pedersen, L. Pedraza-González, Q. M. Phung, K. Pierloot, M. Reiher, I. Schapiro, J. Segarra-Martí, F. Segatta, L. Seijo, S. Sen, D.-C. Sergentu, C. J. Stein, L. Ungur, M. Vacher, A. Valentini and V. Veryazov, *J. Chem. Phys.*, 2020, **152**, 214117.
70 M. Douglas and N. M. Kroll, *Ann. Phys.*, 1974, **82**, 89–155.
71 B. A. Hess, *Phys. Rev. A*, 1985, **32**, 756–763.
72 B. A. Hess, *Phys. Rev. A*, 1986, **33**, 3742–3748.

73 A. Wolf, M. Reiher and B. A. Hess, *J. Chem. Phys.*, 2002, **117**, 9215–9226.
74 L. F. Chibotaru and L. Ungur, *J. Chem. Phys.*, 2012, **137**, 064112.
75 L. Ungur and L. F. Chibotaru, *Inorg. Chem.*, 2016, **55**, 10043–10056.
76 L. F. Chibotaru, *Struct. Bonding*, 2015, **164**, 185–229.
77 D. Aravena, *J. Phys. Chem. Lett.*, 2018, **9**, 5327–5333.
78 B. Yin and C.-C. Li, *Phys. Chem. Chem. Phys.*, 2020, **22**, 9923–9933.
79 B. Yin and L. Luo, *Phys. Chem. Chem. Phys.*, 2021, **23**, 3093–3105.
80 J. Long, A. N. Selikhov, E. Mamontova, K. A. Lyssenko, Y. Guari, J. Larionova and A. A. Trifonov, *Dalton Trans.*, 2019, **48**, 35–39.